Viscous fingering with partially miscible fluids

Xiaojing Fu,[1] Luis Cueto-Felgueroso,[1,2] and Ruben Juanes[1]

[1]*Massachusetts Institute of Technology, 77 Massachusetts Avenue, Building 1, Cambridge, Massachusetts 02139, USA*

[2]*Technical University of Madrid, Calle del Profesor Aranguren 3, 28040 Madrid, Spain*

Viscous fingering—the fluid-mechanical instability that takes place when a low-viscosity fluid displaces a high-viscosity fluid—has traditionally been studied under either fully miscible or fully immiscible fluid systems. Here we study the impact of partial miscibility (a common occurrence in practice) on the fingering dynamics. Through a careful design of the thermodynamic free energy of a binary mixture, we develop a phase-field model of fluid-fluid displacements in a Hele-Shaw cell for the general case in which the two fluids have limited (but nonzero) solubility into one another. We show, by means of high-resolution numerical simulations, that partial miscibility exerts a powerful control on the degree of fingering: fluid dissolution hinders fingering while fluid exsolution enhances fingering. We also show that, as a result of the interplay between compositional exchange and the hydrodynamic pattern-forming process, stronger fingering promotes the system to approach thermodynamic equilibrium more quickly.

I. INTRODUCTION

When a less viscous fluid displaces a more viscous fluid, the contrast in viscosity destabilizes the fluid-fluid interface, leading to the formation of viscous fingers [1–3]. Fluid-fluid miscibility plays an important role in the fingering dynamics, and the fingering pattern can change appreciably based on the miscibility of two fluids. Thus, the subject is traditionally divided into *immiscible* and *miscible* viscous fingering. In both cases, it is viscous forces that drive the hydrodynamic instability. When two fluids are immiscible, surface tension stabilizes short-wavelength perturbations at the interface, allowing some proto-protrusions to spread readily, resulting in less ramified patterns [3–5]. When the two fluids are fully miscible, the absence of surface tension suggests a more intense fingering pattern, as demonstrated by experiments [3,5–7] and simulations [8–12]. Nevertheless, without surface tension, complete suppression of the onset of miscible viscous fingering is possible under certain unfavorable viscosity contrast [6,13] due to three-dimensional (3D) effects. Beyond the onset regime, Ref. [7] has shown that molecular diffusion along the interface leads to shutdown of instability at late times during radial injections. Further, it has been suggested that Korteweg stresses and other nonequilibrium surface tension effects can act to stabilize miscible displacement [14–17].

Despite the conventional categorization into fully immiscible and fully miscible, the miscibility of two fluids can vary based on local conditions such as pressure and temperature [18]. Between the two extremes lie fluid pairs that are *partially miscible*, exhibiting limited, but nonzero, solubility into each other. For such fluid pairs, compositional effects are introduced to two-phase problems where component exchange between phases occurs even in the presence of surface tension. This effect is relevant, for instance, during immiscible gas-in-oil injection for oil recovery where the gas and oil can become partially miscible under high-pressure reservoir conditions, leading to swelling of the oil phase and enhanced recovery [19]. Under this context, the coupling of viscous fingering with thermodynamic effects could provide insights into control of the viscous instability, which has received increased attention in recent studies [12,20–24]. Additionally, addressing the role of compositional effects in low-Reynolds-number two-phase flows is also essential to our understanding of mixing in multiphase mixtures [25], biological cell assembly [26], and geologic sequestration of CO_2 [27].

104001-1

Our current understanding of viscous fingering with partially miscible fluids is very limited. In an effort to address this gap, an experimental study on viscous fingering with partially miscible fluids has been performed recently [28]. The experiments use a ternary system made of water, PEG and Na_2SO_4 to produce viscously contrasting fluid pairs that are fully miscible, immiscible, or partially miscible. The experiments provide an excellent illustration on how thermodynamic effects can exert a powerful control on hydrodynamic instabilities: As the fluid pairs transition from being immiscible to partially miscible, the authors observe that formation of droplets become more common than formation of fingers. The detailed mechanisms behind the droplets formation remain to be understood. On the modeling front, a recent study [29] investigated radial injection under different fluid miscibility conditions using a Darcy-Cahn-Hilliard model, where the fluid miscibility is prescribed through the design of a Cahn-Hilliard-type free energy [30]. Though the model is limited in its ability to explore the truly partially miscible regime, where one would expect to see effects such as finger swelling due to supersaturation, the study provides a consistent comparison between immiscible and miscible viscous fingering to demonstrate the role of compositional effects in controlling the vigor of the instability. As presented in earlier work [7,14], the study confirms that the degree of fingering instability, as measured by interface length, peaks at a transition time, followed by a decay due to diffusive mixing at the interface for *miscible* systems; in *immiscible* simulations, however, where surface tension is present and component diffusion is negligible, a decay in interfacial length is not observed [29].

In this work, we study the interplay between hydrodynamics and nonequilibrium compositional effects in partially miscible systems. To develop insights into the physics of a nonlinear hydrodynamic instability out of thermodynamic equilibrium, here we develop a two-dimensional (2D) gap-averaged model, in the spirit of a large body of literature on Hele-Shaw flows for both miscible and immiscible fluids [8,11,12,20,22,23,31–36]. While a full 3D flow model might be desirable to eventually provide a more detailed description of the flow (as is the case for fully miscible [6,13,37–42] and fully immiscible systems [35,36,43–45]), it should build on the insights of the nonlinear analysis in 2D. We adopt a phase-field modeling approach, which has been successful at describing immiscible two-phase flow in Hele-Shaw geometry [35,36,46–52] and in porous media [53] and, more recently, the coarsening dynamics of partially miscible binary mixtures under viscous fingering [54]. Under the phase-field framework, the design of thermodynamic free energy allows us to readily incorporate partial miscibility into multiphase flow. In its minimal description, the free energy of a two-phase, two-component mixture follows the Cahn-Hilliard form [30], formulated as a functional of component concentration and its gradients. Under the Cahn-Hilliard framework, fluid phase is inferred from component concentration and not independently described. This approach is successful in capturing the dynamics of binary mixtures with fast phase-transition time scale (e.g., immiscible fluids) [29,55–60]. In contrast, our proposed model [54] allows fluid concentrations to evolve independently from the phase variable, in order to capture the essence of *partially miscible* systems, where components can exchange between the two phases at time scales comparable to that of flow. During injection, the evolution of the invading phase variable (e.g., volume fraction of the invading phase) is driven by viscous instability, accompanied by redistribution of composition between phases and phase transformations that are driven by chemical potentials. Capturing the duality of the dynamics requires having separate evolution equations for phase and concentration, and defining a free energy that is a function of both variables. Similar two-field formulations have been extensively adopted for the simulation of binary alloys solidification [61], but, thus far, not for interfacial flows with compositional effects. With this more general framework, we are able to investigate the two-way coupling between hydrodynamics (viscous fingering) and thermodynamics (compositional exchange between phases and phase transformation). We apply our model to the viscous fingering problem in a rectangular Hele-Shaw cell, where initially a gas band is surrounded by a liquid (Fig. 1, left). Gas fingers are then created by pushing the gas band leftward with an imposed constant flux of the liquid phase of the same initial composition (Fig. 1, right).
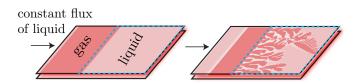
FIG. 1. Displacement of a gas band through liquid phase in a Hele-Shaw cell: (a) initial setup and (b) the displacement leads to viscous fingering due to viscosity contrast. Meanwhile, compositional exchange occurs along the fingering interface if the two fluids are out of thermodynamic equilibrium. For example, in this sample image, the liquid phase is initially supersaturated with respect to gas and will swell the gas fingers as they evolve (see Sec. IV A). The blue dashed box indicates the area of study in our discussions.

II. MATHEMATICAL MODEL

In our recent work [54], we propose a phase-field model of two-phase Darcy flow with two-component transport. Here we provide an extended and detailed description of the model and use it to study the problem described in Fig. 1. Without loss of generality, we focus on a binary mixture that is an analogy for a CO_2 (gas)–water (liquid) system. The two fluids, denoted *gas* (g) and *liquid* (l), have different viscosities with $\mu_l > \mu_g$. Upon contact, they seek to reach compositional equilibrium through mutual component exchange. The result should be a gas phase that is rich in the primary component (e.g., CO_2) and a liquid that is rich in the secondary component (e.g., H_2O). We introduce two variables, defined pointwise, to describe the state of the binary mixture: the gas volume fraction, ϕ, is a nonconserved quantity due to dissolution and/or expansion of the gas phase; the molar fraction of CO_2, c, is conservative in the entire domain. The model describes the evolution of ϕ and c when the binary mixture is subjected to hydrodynamic instabilities.

A. Phase-field modeling of two-phase Darcy flow with compositional effects

We introduce the following dimensional governing equations to describe incompressible, isothermal, two-phase flow with two-component transport in a Hele-Shaw cell, with a uniform gap thickness b:

$$\nabla \cdot \mathbf{u} = 0, \quad \mathbf{u} = -\frac{k}{\mu(\phi)} \nabla P, \tag{1}$$

$$\frac{\partial \phi}{\partial t} + \nabla \cdot (\mathbf{u}\phi) + \lambda^\phi \Psi_\phi = 0; \tag{2}$$

$$\frac{\partial c}{\partial t} + \nabla \cdot (\mathbf{u}c) - \nabla \cdot (\lambda^c \nabla \Psi_c) = 0. \tag{3}$$

Equations (1) are the continuity equation for an incompressible mixture and Darcy's law, where $\mathbf{u}$ is the mixture velocity, P is a kinematic pressure, k is a constant permeability, and μ is the mixture viscosity, assumed to follow an exponential dependence on phase fraction, $\mu(\phi) = \mu_g \exp[R(1 - \phi)]$, where $R = \log(\mu_l/\mu_g)$ is the viscosity contrast.

In the context of phase-field modeling, we understand ϕ also as a phase variable, which takes a value of 1 in the gas and 0 in the liquid, and interpolates smoothly between the two bulk phases over a well-resolved, diffuse numerical interface. Time evolution of ϕ simulates gas dissolution and/or exsolution [Eq. (2)], and can be considered a relaxation process toward a minimum of the free energy function of the system F [62]. The gradient toward minimization, obtained by taking the variational derivative of F with respect to ϕ, can be understood as a phase potential that drives phase transformations:

$$\Psi_\phi \equiv \delta F/\delta\phi = \partial F/\partial\phi - \nabla \cdot [\partial F/\partial(\nabla\phi)]. \tag{4}$$

The dynamics of phase transformation [Eq. (2)] are formulated using Allen-Cahn dynamics [63]. The evolution of c is described by a nonlinear advection-diffusion equation [Eq. (13)], where the component diffusion is driven by gradients in chemical potentials, defined similarly to Eq. (4):

$$\Psi_c \equiv \delta F / \delta c = \partial F / \partial c - \nabla \cdot [\partial F / \partial (\nabla c)]. \tag{5}$$

In Eqs. (2) and (3), λ^ϕ and λ^c are mobilities for ϕ and c respectively. Here we assume that both mobilities are only a function of c:

$$\lambda^\phi b^2 = \lambda^c = \frac{D/\nu}{R_{\text{ideal}}T}[c(1-c) + 0.01], \tag{6}$$

where D is the diffusion coefficient, ν is the molar density, R_{ideal} is the ideal gas constant, and T is temperature (assumed constant here). We define the characteristic composition mobility as

$$\lambda_c = \frac{D/\nu}{R_{\text{ideal}}T} \tag{7}$$

and the characteristic phase mobility as

$$\lambda_c^\phi = \frac{D/\nu}{b^2 R_{\text{ideal}}T}. \tag{8}$$

B. Design of free energy

The free energy functional $F(\phi,c)$ plays a central role in the thermodynamic behavior of our binary mixture. Following the classical Cahn-Hilliard formulation for a binary system [30], our F subsumes interfacial and bulk energy contributions:

$$F(\phi,c) = \int_V \left[\frac{1}{2}\epsilon_\phi^2 T(\nabla\phi)^2 + \frac{1}{2}\epsilon_c^2 T(\nabla c)^2 + \omega T W(\phi) + \omega_{\text{mix}}T\{f_l(c)[1 - g(\phi)] + f_g(c)g(\phi)\} \right] dV. \tag{9}$$

The first two terms in Eq. (9) capture the interfacial energy associated with phase and compositional boundaries. The characteristic interfacial energies per unit volume associated with ϕ and c are $\epsilon_\phi^2 T$ and $\epsilon_c^2 T$ respectively. The third term is the part of the bulk free energy responsible for phase separation, where $W(\phi) = \frac{1}{4}\phi^2(1-\phi)^2$ adopts the shape of a double well, determining the two stable states of F: $\phi = 0$ or $\phi = 1$. Here, ω is the energy (per unit volume) associated with the double-well energy. The last term, known as the bulk mixing energy, is the part of the bulk free energy responsible for partially miscible behavior. We adopt a form for mixing energy that is commonly used in the field of binary alloy solidification [64], where the energy is an interpolation in ϕ between liquid and gas excess energies (f_l and f_g), which are functions of c only. Here, $\omega_{\text{mix}}T$ is the energy (per unit volume) associated with mixing. The interpolation function $g(\phi) = -\phi^2(2\phi - 3)$ satisfies that the system approaches the stable states $\phi = 0,1$ with zero slope, which ensures positivity of the phase variable [64]. The excess free energy of each phase are due to compositional effects; here we adopt the Wilson model [65]:

$$f_l(c) = c \log c + (1 - c)\log(1 - c) - c \log(c + \alpha_l(1 - c)) - (1 - c)\log(1 - c + \beta_l c),$$
$$f_g(c) = c \log c + (1 - c)\log(1 - c) - c \log[c + \alpha_g(1 - c)] - (1 - c)\log(1 - c + \beta_g c), \tag{10}$$

where α_l, α_g, β_l, and β_g are assigned parameters. The equilibrium concentrations within each phase are then obtained by the common tangent construction of f_l and f_g [66,67] (Fig. 2). Note here that both $f_l(c)$ and $f_g(c)$ are dimensionless.
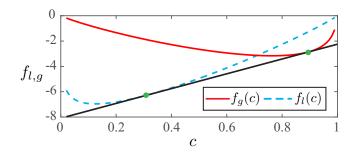
FIG. 2. Common tangent construction: Here we assign the parameters in Eq. (10) as $\alpha_l = 2 \times 10^{-7}$, $\beta_l = 2 \times 10^4$, $\alpha_g = 200$, $\beta_g = 2 \times 10^{-4}$ so that the common tangent construction yields the equilibrium composition of the two fluids: $c_g^{eq} \approx 0.89$, $c_l^{eq} \approx 0.33$.

C. Scaling analysis

We identify the following characteristic scales in our system: $\epsilon_\phi^2 T / b^2$ is the characteristic energy, b is the length scale, and $t_c = b/u_c$ is the characteristic time with $u_c = (k_c \Delta p_c)/(\mu_g b)$, where k_c, Δp_c are the characteristic permeability and pressure drop respectively. Additionally, we introduce λ_c as the characteristic composition mobility [Eq. (7)] and λ_c^ϕ as the characteristic phase mobility [Eq. (8)]. In its dimensionless form, the system of equations reads

$$\nabla \cdot \mathbf{u} = 0, \quad \mathbf{u} = -\frac{1}{\mu(\phi)} \nabla P, \tag{11}$$

$$\frac{\partial \phi}{\partial t} + \nabla \cdot (\mathbf{u}\phi) + \frac{1}{\mathrm{Ca}} \lambda \Psi_\phi = 0, \tag{12}$$

$$\frac{\partial c}{\partial t} + \nabla \cdot (\mathbf{u}c) - \frac{1}{\mathrm{Pe}} \nabla \cdot (\lambda \nabla \Psi_c) = 0, \tag{13}$$

where $\mu(\phi) = e^{R(1-\phi)}$ and $\lambda = 0.01 + c(1-c)$. The first dimensionless group, the capillary number Ca, sets the ratio between time scales associated with phase change and advection:

$$\mathrm{Ca} = (u_c b)/(\lambda_c^\phi \epsilon_\phi^2 T), \tag{14}$$

where $\epsilon_\phi^2 T/b$ is the interfacial tension. We expect that Ca controls the characteristic length scale of the instability pattern, such that the characteristic length decreases with increasing Ca [54]. The second dimensionless group, the Péclet number, sets the ratio between rate of advection and diffusion:

$$\mathrm{Pe} = (u_c b)/(\lambda_c \epsilon_\phi^2 T). \tag{15}$$

Pe controls the rate of diffusion within a single phase, and therefore directly affects the rate of gas dissolution and/or exsolution. We expect that for large values of Pe, the finger morphology will approach that of an immiscible system. In dimensionless form, the free energy is described with three additional dimensionless groups:

$$F(\phi, c) = \int_V \left[\frac{1}{2}(\nabla\phi)^2 + \epsilon \frac{1}{2}(\nabla c)^2 + \frac{1}{\mathrm{Ch}}W(\phi) + \frac{1}{\mathrm{Ma}}\{f_l(c)[1 - g(\phi)] + f_g(c)g(\phi)\} \right] dV. \tag{16}$$

We introduce the third dimensionless group as the ratio between the two energy scales associated with compositional and phase boundaries:

$$\epsilon = \epsilon_c^2/\epsilon_\phi^2. \tag{17}$$

An increase in ϵ would mean that the numerical profile of concentration (c) becomes sharper and the numerical profile of phases (ϕ) becomes smoother. The fourth group is the Cahn number, which controls the thickness of the numerical interface:

$$\text{Ch} = \left(\epsilon_\phi^2/b^2\right)/\omega. \tag{18}$$

A larger Ch would require more grid points to resolve the fluid-fluid interface. Phenomenologically, a larger Ch also corresponds to a system with larger surface tension. Finally, we define a solutal Marangoni number, which sets the ratio between interfacial energy and mixing energy:

$$\text{Ma} = \left(\epsilon_\phi^2/b^2\right)/\omega_{\text{mix}}. \tag{19}$$

As Ma increases, the system becomes dominated by interfacial effects and we expect nonequilibrium thermodynamics to play a weaker role in the pattern-forming process.

III. PROBLEM SETUP AND NUMERICAL METHODS

We conduct high-resolution numerical simulations of our model for the problem described in Fig. 1, in which we displace a band of less viscous gas through the more viscous ambient liquid under a constant flux of liquid of the same initial composition. Our simulations are on a domain of size 200×80 ($L_x \times L_y$) and parameter values Ch $= 1/2000$, Ma $= 1/200$, and $\epsilon = 200$ (and parameters of the Wilson model given in Fig. 2). We perform a straightforward calculation of Ca and Pe in order to mimic an experimental fluid pairs analogous to water and methane gas (weakly soluble in water). We approximate the typical injection rate in a rectilinear geometry to be $U = 1.9 \times 10^{-3}$cm/s, based on the values reported in Ref. [44]. The surface tension is take as that of water and air at room temperature: $\epsilon_\phi^2 T/b = 72$ dyn/cm. The diffusion coefficient of gas in water at $25°$ is taken from Ref. [68] as $D = 2 \times 10^{-5}$ cm^2/s. The molar density of pure water is about 0.056 mol/cm^3 and that of gas is about 0.00005 mol/cm^3. Here we take an intermediate value of 0.01 mol/cm^3 for ν. Based on these values, we calculate that $\lambda_c^\phi = 1.29 \times 10^{-5}$ cm^3/($J\,s$) and $\lambda_c = 8.1 \times 10^{-7}$ cm^5/($J\,s$). The key dimensionless parameters in our system are computed as Ca $= U/(\lambda_c^\phi \gamma) \approx 2$ and Pe $= U/\lambda_c \gamma \approx 32$.

We are interested in exploring the coupling between hydrodynamic instabilities and thermodynamic effects. Consequentially, we focus on two parameters, each of which controls one aspect of the coupling: (a) the viscosity contrast R between the two fluids and (b) the initial composition of the liquid phase c_l^0. The parameter R is chosen here to be $R = 0, 1, 2, 3, 4$, and 5, where the gas phase is always less (or equally) viscous than the liquid. The value of c_l^0 determines the thermodynamic response of the two fluids when interacting, where three scenarios may occur: (i) the gas dissolves, transferring CO_2 into the liquid; (ii) the gas and liquid are at equilibrium, no component exchange occurs; or (iii) the gas expands in volume by exsolving CO_2 from the liquid. As shown in Fig. 2, the common tangent construction of the bulk free energies yields the equilibrium composition of the two fluids as $c_g^{\text{eq}} \approx 0.89, c_l^{\text{eq}} \approx 0.33$. Instructed by this calculation, we can recreate the three scenarios by setting the defending liquid to be initially (at $t = 0$)

 (a) *undersaturated* with respect to the gas phase: $c_l^0 = 0.05 < c_l^{\text{eq}}$;
 (b) *near saturated* with respect to the gas phase: $c_l^0 = 0.33 \approx c_l^{\text{eq}}$;
 (c) *supersaturated* with respect to the gas phase: $c_l^0 = 0.5 > c_l^{\text{eq}}$.

In all the simulations performed, we only vary R and c_l^0 while all other parameters are unchanged. We initialize the gas phase with a composition that is close to equilibrium values: $c_g^0 = 0.89 \approx c_g^{\text{eq}}$. Further, all simulations start with the same initial configuration in ϕ (as shown in Fig. 1 left):

$$\phi_0 = \begin{cases} 1, & \text{if } 0.05L_x \leqslant x \leqslant 0.4L_x \\ 0, & \text{otherwise} \end{cases}. \tag{20}$$

The initial concentration field c_0 is computed as an affine mapping from ϕ_0:

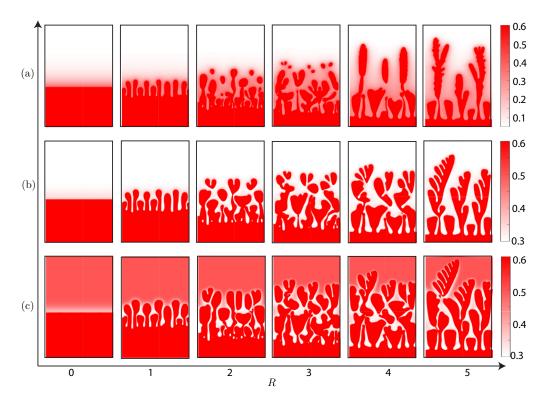$$c_0 = \left(c_l^0 - c_g^0\right)(1 - \phi_0) + c_g^0. \tag{21}$$

FIG. 3. The coupling between different viscosity contrast and compositional effects leads to a rich set of viscous fingering patterns. Here we show snapshots of c at $t = 50$ for six different R values (across each row). Each of the three rows correspond to different c_l^0 values: defending liquid is (a) undersaturated ($c_l^0 = 0.05$), (b) near saturated ($c_l^0 = 0.33$), and (c) oversaturated ($c_l^0 = 0.5$). Note that the color map differs between each row to reveal the detailed structures in the concentration field.

We solve Eqs. (11)–(13) sequentially. We first obtain the pressure and velocity using a finite volume method with a two-point flux approximation. Next we update c and ϕ using a Fourier pseudospectral discretization and a biharmonic-modified time stepping [69]. The domain is discretized with 2560×1024 ($N_x \times N_y$) points. The boundary conditions are periodic, but we show results only in a window of the simulation domain ($80 \leqslant L_x \leqslant 200$, indicated as the blue dashed box in Fig. 1) unaffected by the boundaries during the simulation period reported (that is, until the fingers reach the right boundary).

IV. RESULTS

A. Fingering pattern under the influence of gas dissolution and exsolution

We present a summary of the final displacement pattern (in c) in a $c_l^0 - R$ phase diagram in Fig. 3. The middle row of the phase diagram corresponds to a displacement scenario where the two fluids are near saturated, analogous to immiscible displacement [4,70]. In this regime, viscosity ratio is understood as the control parameter for large-scale structure of the pattern [2,71]. With this series of simulations, we recover the classic features of immiscible viscous fingering: shielding, spreading, and tip splitting [2], as well as side branching, merging, pinchoff of fingers, and entrapment of the defending phase toward the injection side [72,73]. The rest of the phase diagram (top and bottom rows) illustrates the effects of gas dissolution and/or exsolution on the displacement patterns.
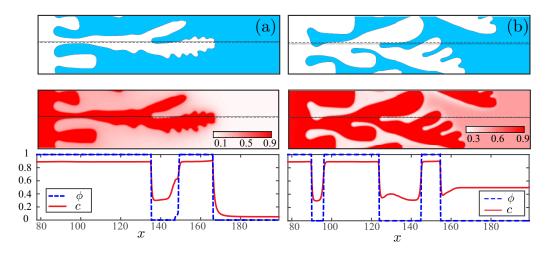
FIG. 4. Defending fluid is (a) undersaturated or (b) supersaturated. Top: snapshots of ϕ at $t = 46$. Middle: snapshots of c at $t = 46$. Bottom: horizontal transects of ϕ (dashed) and c (solid) at $t = 46$ along the dashed lines indicated in the 2D plots in the top and middle rows. Note that regions where $c \approx 0.33$ indicate areas in which local thermodynamic equilibrium is in place.

In the top row, the defending liquid is undersaturated with respect to the gas. Upon contact, the gas volume dissolves locally to replenish the CO_2 concentration level in the ambient liquid. This dissolution process hinders the growth of young fingers, or proto-protrusions, that form along the sides of dominant fingers. By immediately stripping away any gas accumulation that fuels the growth of instability, the dissolution process inhibits protoprotrusions from developing into mature fingers. As a result, it has significantly weakened development of side branches as well as the shielding and merging processes. The dissolution effect is most active toward the front of the invasion, where the gas phase is persistently met with undersaturated liquid. Under this effect, the unbifurcated fingers appear slimmer ($R = 1$), and we observe disconnected droplets that become rounded due to dissolution for intermediate viscosity contrast ($R = 2,3$); for larger viscosity contrast ($R = 4,5$), we observe "bald" dominant fingers that lack active side branches.

An important distinction between partially and fully miscible fluids pair is the direction of component diffusion. In a fully miscible system, molecular diffusion of the components follow the direction of positive concentration gradient. In the case of partially miscible fluids, however, component diffusion is directed in the direction of chemical potential gradient, which can sometimes be the reverse of the concentration gradient. Such is the case when the gas phase is exposed to an oversaturated liquid (bottom row of the phase diagram), where the invading fingers swell by exsolving the excess CO_2 from the liquid, against the direction of concentration gradient. Exsolution into the gas phase increases the volume of gas (ϕ) and thus promotes instability in the system as it expands the radius of invading front for tip splitting [4]. This results in an enhanced shielding and merging effect and more prominent side branches. Such promotion of instability is observed across all values of R where fingering occurs, and the effect is most apparent for $R = 4,5$. In addition, the fingers also appear larger overall in comparison to the middle row.

B. The coupling between ϕ and c

We illustrate the fingering pattern using the c field in Fig. 3; however, it is important to note that both ϕ and c are independently solved using separate evolution equations in our model. To demonstrate this, Fig. 4 shows snapshots of 1D cross section profiles of both ϕ and c side by side for $R = 5$ with *unsaturated* (left) and *oversaturated* (right) defending fluid. From this, we observe that both ϕ and c, although independently solved, follow each other closely. The pattern in c emulates
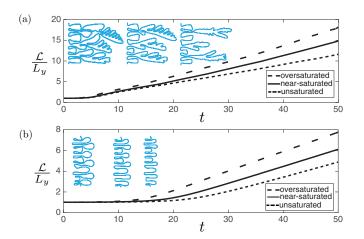
FIG. 5. Normalized interfacial length, $\mathcal{L}/L_y$, as a function of time for three compositional scenarios with (a) $R = 5$ and (b) $R = 1$. In both plots, colored insets show the traced outline of the fingering front at $t = 50$ for oversaturated, near-saturated, and unsaturated defending liquid (left to right).

that of ϕ, although c provides more details on component distribution within each phase. There are, however, fundamental differences in how these two variables behave under their own evolution equation. The one-dimensional (1D) profile of ϕ (Fig. 4 bottom, dashed blue line) is continuous but compact—a feature of immiscible invasion under diffuse-interface descriptions. Meanwhile, the 1D profile of c (Fig. 4 bottom, solid red line) exhibits a diffuse profile that is inherent to diffusive component transport. The coupling between ϕ and c is not merely a modeling construct: Rather, it provides compositional details of the two-phase system that either variable alone would not be able to reveal. This is further discussed in Sec. IV E.

C. Thermodynamic control on the degree of fingering

Thermodynamic effects such as chemical reactions can lead to a myriad of interesting behaviors when coupled with hydrodynamic instabilities [24,74–77]. In this work, we explore such coupling in the form of thermodynamics-driven phase transformation that leads to finger dissolution and exsolution during viscous fingering. The coupling can be of particular interest in the context of controlling of the viscous instability, which has received increased attention in recent studies [12,20–24]. Proposed mechanisms include using chemical reactions [24], alternating injections [12], controling injection rate [20,78], imposing a gradient in flow pathway [22,79], or confining the flow by elastic membranes [23].

In Sec. IV A, we demonstrate qualitatively that thermodynamic-driven phase transformations, resulting in fluid dissolution or exsolution, can hinder or enhance viscous fingering instabilities beyond onset regime. Here we quantify such effect by inferring the degree of fingering with direct measurement of the total interfacial length generated by the instability, using image segmentation (see examples in Fig. 5 insets). The interfacial length of the fingering front, $\mathcal{L}$, is scaled by the transversal domain length, $L_y = 80$, so that initially $\mathcal{L}/L_y = 1$ and will increase as fingers form and grow (Fig. 5). When $R = 0$, $\mathcal{L}/L_y = 1$ for the entirety of the simulation. In Fig. 5, we show the evolution of $\mathcal{L}/L_y$ under $R = 1$ (bottom) and $R = 5$ (top) for all three compositional scenarios. The degree of fingering persistently increases under all scenarios; the instability is not suppressed due to gas dissolution. However, compared to the second scenario (the immiscible analog, solid lines), the interfacial growth is slowed down under gas dissolution (short dashed line), indicating weakening of the instability; on the other hand, the growth is significant enhanced under finger swelling (long dashed line), indicating promotion of the instability.
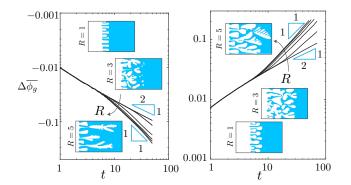
FIG. 6. $\Delta\overline{\phi_g}(t)$ for $R = 0,1,2,3,4,5$ (arrows indicating increasing order) when the defending phase is undersaturated (left) and supersaturated (right). The insets in both plots show snapshots of ϕ at $t = 50$ for the different values of R.

The insets in Fig. 5(b) also illustrate a greater finger competition for the oversaturated case. This is due to the fact that under an oversaturated scenario, gas exsolution leads to finger swelling and a space-fling competition that promotes of some fingers while suppressing some others. This enhanced competition is not observed for the unsaturated cases at $R = 1$.

D. Impact of viscous fingering on the rate of gas dissolution and/or exsolution

The total gas volume fraction in the system should decrease due to gas dissolution or increase due to gas exsolution. In other words, the amount of gas volume change in the domain is a global measure that reflects how much the system has progressed toward thermodynamic equilibrium.

Locally, the reduction or increase in gas volume is a direct consequence of component exchange across the phase-phase boundary. We expect that hydrodynamic instability will play an important role in this process because phase transformations take place at the invasion front where the two fluids are out of equilibrium, and viscous fingering deforms and lengthens such front.

Here, we define the change in gas volume fraction across the whole domain over time as

$$\Delta\overline{\phi_g}(t) = \frac{\iint \phi(t)dxdy - \iint \phi_0 dxdy}{\iint \phi_0 dxdy}. \tag{22}$$

In Fig. 6, we show $\Delta\overline{\phi_g}(t)$ for different values of R when the defending fluid is undersaturated (left) and supersaturated (right). When no viscosity contrast is present ($R = 0$), the invasion front remains stable and phase transformation is limited by the rate at which CO_2 diffuses in the liquid phase in order to be transported away or toward the gas phase. This explains $|\Delta\overline{\phi_g}| \sim t^{1/2}$ for $R = 0$ in both composition scenarios. In the presence of the hydrodynamic instability ($R > 0$), the invasion-front deformation provides more interfacial area over which the two fluids can equilibrate. This mass-transfer enhancement is clearly shown in the scaling $|\Delta\overline{\phi_g}| \sim t^1$, observed for $R = 2,3,4,5$.

E. Heterogeneity in phase compositions

While gas volume fraction is a measure of how the system progresses toward its thermodynamic equilibrium globally, here we show that progress toward equilibrium can be very heterogeneous within the domain. To do this, we track the liquid phase concentration, computed pointwise as

$$c_l(x,y) = [1 - \phi(x,y)]c(x,y). \tag{23}$$

We introduce $\overline{c_l}_y(x)$ as the y-averaged liquid phase concentration along the x axis. If a thermodynamic equilibrium is reached locally, $\overline{c_l}_y \approx c_l^{eq}$ at that point; otherwise, $\overline{c_l}_y$ should be larger or smaller than
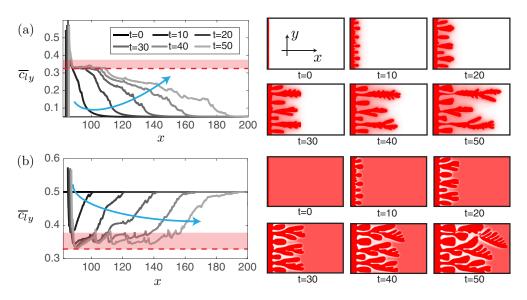
FIG. 7. (Left) $\overline{c}_{l_y}(x)$ at $t = 0$, 10, 20, 30, 40, and 50. Blue arrow indicates direction of time. Red dashed line indicates thermodynamic equilibrium: $c_l^{\text{eq}} \approx 0.33$. Red shaded area indicates metastability. (Right) Snapshots of c for the corresponding times. The defending liquid is initially undersaturated in panel (a) and supersaturated in panel (b), and all simulations correspond to $R = 5$.

c_l^{eq}. In Fig. 7 (left column), we plot $\overline{c}_{l_y}(x)$ at six different times with $R = 5$ for undersaturated [Fig. 7(a)] and supersaturated [Fig. 7(b)] defending liquid. The shaded red region indicates *metastability*, where the system is close to thermodynamic equilibrium (red dashed lines in Fig. 7). From this, we observe that the system reaches metastability toward the roots of the fingers, where two fluids have more time to equilibrate. Toward the fingering front, the fluid-fluid interface is newly created, leaving little time for component exchange to occur; therefore, the liquid composition appears to be far away from thermodynamic equilibrium at the fingering front. The spatial heterogeneity in the phase compositions and consequently in the thermodynamic equilibrium state between the fluids has implications on the pattern-forming process: Toward the roots of the fingers, where the system has established a thermodynamic equilibrium earlier, the fingering morphology is no longer subject to dissolution and/or exsolution effects; toward the invasion front, freshly created fingers are subject to constant shrinkage and/or expansion due to gas dissolution and/or exsolution.

F. Fingering pattern as controlled by Ch and Ma

The Cahn number (Ch) controls the effective surface tension between the two fluids. As Ch increases, the system experiences increasing surface tension. Here we verify this effect by simulating viscous fingering at four different values of Ch at a fixed Ma $= 1/200$ (all other parameters are kept the same as introduced in Sec. III). The results as shown in Fig. 8 demonstrate that as Ch increases from left to right, an increasing surface tension results in more prominent finger pinchoff.

The solutal Marangoni number (Ma) controls the thermodynamic forcing that leads to partial miscibility. It appears as a coefficient of the chemical potential, which is defined as

$$\Psi_c = \epsilon \nabla^2 c + \frac{1}{\text{Ma}} \{ f_l'(c)[1 - g(\phi)] + f_g'(c)g(\phi) \}. \tag{24}$$

Although Ma does not change the compositional equilibrium, one can treat 1/Ma as a kinetic rate coefficient that drives component diffusion within each phase. Such diffusion is proportional to the gradient in Ψ_c and will diminish as the system approaches equilibrium (the expression multiplied by 1/Ma will be zero at equilibrium). As Ma increases, the rate of diffusion decreases within each
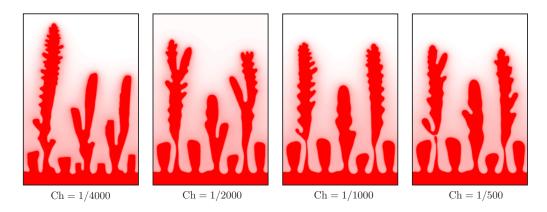
FIG. 8. Impact of Cahn number at Ma = 1/200 and other parameters kept the same as in Sec. III. We simulate for four values of Ch differing by a factor of two each. Shown here are snapshots of c at $t = 40$. The color-map range is [0.05,0.9] for all figures.

phase and the system takes longer to reach compositional equilibrium. This effect is confirmed by Fig. 9, where we see that as Ma increases from left to right, the liquid phase composition is more heterogeneous and farther away from equilibrium (supersaturated in many regions for Ma = 1/50 and 1/25).

It is also important to note that a decrease in 1/Ma also indirectly promotes the strength of surface tension in the system. This is due to the structure of the free energy design [Eq. (16)]. As a result, an increase in Ma indicates an increase in surface tension, allowing the system to favor more pinchoff and tip-splitting events (Fig. 9). Such nonlinear interactions between compositional effects and fluid instability lead to interesting dynamics in fluid mixing. Here, we use the variance of the concentration field to measure fluid mixing:

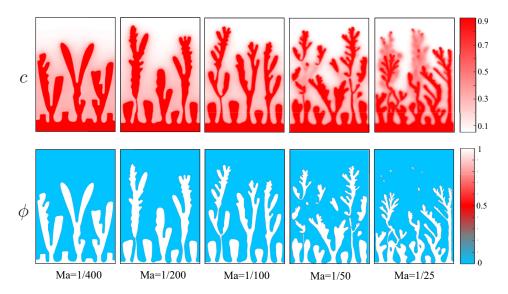$$\sigma^2 = \langle c^2 \rangle - \langle c \rangle^2. \tag{25}$$

FIG. 9. Impact of solutal Marangoni number at Ch = 1/2000 and other parameters kept the same as in Sec. III. We simulate for five values of Ma differing by a factor of two each. Shown here are snapshots of c (top) and ϕ (bottom) at $t = 50$.
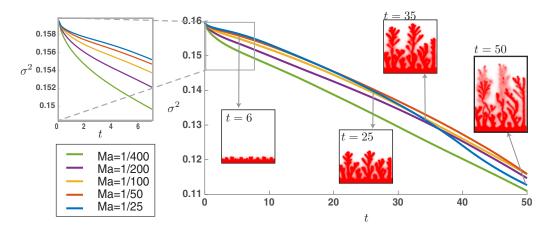
FIG. 10. Concentration variance σ^2 as a function of time for different values of Ma. The enlarged portion on the left corresponds to the early time regime when the fluid interface has not been significantly destabilized. The insets in the main figure correspond to snapshots of c for the Ma $= 1/25$ simulation.

In Fig. 10, we study the effect of Ma on fluid mixing by analyzing the temporal dynamics of σ^2 from the set of simulations shown in Fig. 9. We conclude that the rate of mixing is initially enhanced by smaller Ma (enlarged figure to the left), which is consistent with the implication from Eq. (24). However, as a result of nonlinear coupling between fingering instability and dissolution effects, a larger Ma (e.g., Ma $= 1/25$) produces significantly more tip-splitting and pinchoff events, which results in the creation of more interfacial area and faster mixing at later times (Fig. 10, $t > 20$).

G. Fingering pattern with decreasing miscibility gap

The miscibility gap of a fluids pair is defined here as the difference in compositions between the two fluids once they reach compositional equilibrium: $c_g^{\text{eq}} - c_l^{\text{eq}}$. In our current model, the miscibility gap is determined solely by the description of the bulk mixing energy functions $f_l(c)$ and $f_g(c)$. By changing the parameter values in Eq. (10), we explore the ability of our model framework to describe fluid pairs with different levels of partial miscibility. We stress here that the miscibility gap is determined solely by the shape of the bulk mixing energy curves $f_l(c)$ and $f_g(c)$; tuning the parameters Ma, Ch, ϵ, Pe, and Ca will only change the dynamics as the system approaches equilibrium.

In Fig. 11, we explore the pattern-forming dynamics as we inject fluid pairs with a different miscibility gap. This is done by tuning the parameters (α_l, α_g, β_l, and β_g) in the bulk-mixing energy curves of each phase [Eq. (10)]. As we close the miscibility gap (top to bottom), we also change the initial condition in concentration so that the liquid phase is always undersaturated and the gas phase is at saturation. Specifically,

(i) The top row corresponds to the majority of the simulations discussed in this work, where $\alpha_l = 2 \times 10^{-7}$, $\beta_l = 2 \times 10^4$, $\alpha_g = 200$, $\beta_g = 2 \times 10^{-4}$ so that the common tangent construction yields the equilibrium composition of the two fluids: $c_g^{\text{eq}} \approx 0.89$, $c_l^{\text{eq}} \approx 0.33$.

(ii) The middle row corresponds to $\alpha_l = 20$, $\beta_l = 200$, $\alpha_g = 200$, $\beta_g = 20$ so that the common tangent construction yields the equilibrium composition of the two fluids: $c_g^{\text{eq}} \approx 0.65$, $c_l^{\text{eq}} \approx 0.35$.

(iii) The bottom row corresponds to $\alpha_l = 100$, $\beta_l = 200$, $\alpha_g = 200$, $\beta_g = 100$ so that the common tangent construction yields the equilibrium composition of the two fluids: $c_g^{\text{eq}} \approx 0.55$, $c_l^{\text{eq}} \approx 0.45$.

We keep all the other parameters the same as introduced in Sec. III. In Fig. 11, we observe that even as the miscibility gap narrows (approaching the fully miscible limit), where one might expect a transition to a miscible viscous fingering pattern [11], the system always exhibits the effect of interfacial tension and the fingering pattern resembles that of immiscible displacement. This effect
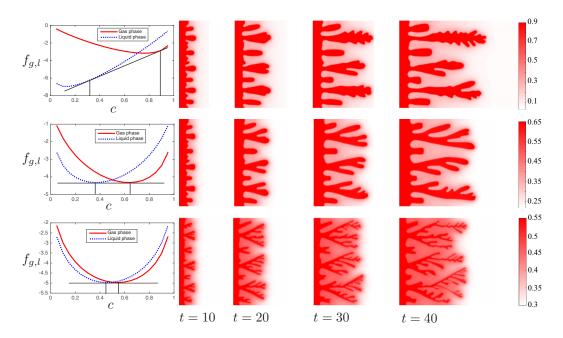
FIG. 11. Impact of miscibility gap in the bulk-mixing energy curves. (Left): $f_l(c)$ and $f_g(c)$ and their common tangent constructions. (Right) Snapshots of c from simulations using the bulk-mixing energy described in the left column. Note that the color-map ranges are different and correspond to the initial composition (slightly wider than miscibility gap).

is due to our simplified description of mixture viscosity and surface tension. Currently, viscosity in our model is a function of ϕ only, and the effective surface tension is independent of fluid composition. Incorporating a more sophisticated design of viscosity as a function of both ϕ and c and a concentration-dependent surface tension term may allow our model to capture more accurately the transitions towards the fully miscible limit. Nevertheless, the model is robust in capturing the correct thermodynamics, where the fluids arrive at their respective equilibrium compositions as predicted by the bulk mixing energy curves in all three cases.

V. CONCLUSIONS

In this paper, we study viscous fingering with partially miscible fluids. We introduce a phase-field model to describe two-phase two-component flow and transport in a Hele-Shaw cell. We present high-resolution numerical simulations of the model applied to the viscous fingering problem for various viscosity contrasts and different initial fluid compositions. From the perspective of pattern formation, our results demonstrate that fluid dissolution or exsolution due to partial miscibility can hinder or enhance viscous fingering, respectively. This is shown by both directly visualizing the fingering pattern (Sec. IV A) and also by quantifying the degree of fingering through the measure of interfacial length (Sec. IV C).

Conversely, we also explore how the pattern-forming process can impact the rate at which the two fluids reach compositional equilibrium. By measuring globally the amount of gas dissolution and/or expansion from component mass transfer, we show that the increase in degree of fingering—and associated increase in interfacial length—is directly linked to a faster rate of thermodynamic equilibration (Sec. IV D). By measuring locally the degree of equilibrium, we show that equilibrium is reached earlier toward the roots of the fingers, where the two fluids have more time to exchange components (Sec. IV E). The spatial heterogeneity in the degree of thermodynamic equilibrium implies that the gas fingers are subjected to different levels of dissolution and/or expansion

effects throughout the domain. As a result, the final fingering pattern we observe is a result of the complex nonlinear coupling between hydrodynamic instabilities and thermodynamic effects. Through additional simulations in Sec. IV F, we show that both Ch and Ma can affect the fingering pattern. As Ch increases, the system experiences increasing surface tension and more pinchoff events. As Ma increases, the system takes longer to reach compositional equilibrium and the liquid composition appears more heterogeneous. Further, because a larger Ma also indirectly promotes the strength of surface tension, we also observe more tip-splitting and pinchoff events at larger Ma. Such nonlinear coupling between fingering instability and dissolution effects results in a nonmonotonic trend in mixing efficiency as a function of Ma.

An important assumption we make in this paper is that the thermodynamically driven component exchange does not change the density or viscosity of either fluid, or the interfacial tension between the two phases. This assumption allows us to simplify the parameter space for our simulations and thus focus on the effect of viscosity contrast and initial fluid compositions. However, these assumptions may no longer be valid for realistic fluid pairs where density, viscosity, and interfacial tension can change appreciably due to mass transfer across phases. As explained in Sec. IV G, our current model does not reproduce miscible viscous fingering pattern as we close the miscibility gap; surface tension plays a significant role in the fingering instability for all values of fluid miscibility gap in our model. We attribute this to an oversimplified design of viscosity and surface tension, which we plan to extend in future work. Further, the effect of component exchange on fluid properties could yield interesting displacement dynamics. For instance, while we only explore the displacement dynamics under a viscously unstable configuration ($R > 0$) in this work, unstable displacement could still arise under an initially viscously stable configuration ($R < 0$). Under constant fluid-fluid component exchange, this instability could be caused by, for example, nonuniform changes in local surface tension at the fluid interface (a Marangoni effect) or changes in local fluid viscosity that eventually reverse the viscosity contrast. It would be interesting to incorporate these effects in our current model in the future to fully understand ongoing experimental studies [28].

---

[1] P. G. Saffman and G. I. Taylor, The penetration of a fluid into a porous medium or Hele-Shaw cell containing a more viscous liquid, Proc. R. Soc. London, Ser. A **245**, 312 (1958).

[2] G. M. Homsy, Viscous fingering in porous media, Annu. Rev. Fluid Mech. **19**, 271 (1987).

[3] J.-D. Chen, Fingering in Hele-Shaw cells, Exp. Fluids **5**, 363 (1987).

[4] L. Paterson, Radial fingering in a Hele-Shaw cell, J. Fluid Mech. **113**, 513 (1981).

[5] J.-D. Chen, Growth of radial viscous fingers in a Hele-Shaw cell, J. Fluid Mech. **201**, 223 (1989).

[6] I. Bischofberger, R. Ramachandran, and S. R. Nagel, Fingering versus stability in the limit of zero interfacial tension, Nat. Commun. **5**, 5265 (2014).

[7] J. Y.-Y. Chui, P. de Anna, and R. Juanes, Interface evolution during radial miscible viscous fingering, Phys. Rev. E **92**, 041003 (2015).

[8] C. T. Tan and G. M. Homsy, Simulation of nonlinear viscous fingering in miscible displacement, Phys. Fluids **31**, 1330 (1988).

[9] C.-Y. Chen and E. Meiburg, Miscible porous media displacements in the quarter five-spot configuration, part 1: The homogeneous case, J. Fluid Mech. **371**, 233 (1998).

[10] A. Riaz and E. Meiburg, Three-dimensional miscible displacement simulations in homogeneous porous media with gravity override, J. Fluid Mech. **494**, 95 (2003).

[11] B. Jha, L. Cueto-Felgueroso, and R. Juanes, Fluid Mixing from Viscous Fingering, Phys. Rev. Lett. **106**, 194502 (2011).

[12] B. Jha, L. Cueto-Felgueroso, and R. Juanes, Synergetic Fluid Mixing from Viscous Fingering and Alternating Injection, Phys. Rev. Lett. **111**, 144501 (2013).

[13] E. Lajeunesse, J. Martin, N. Rakotomalala, and D. Salin, 3D Instability of Miscible Displacements in a Hele-Shaw Cell, Phys. Rev. Lett. **79**, 5254 (1997).

[14] C.-Y. Chen, L. Wang, and E. Meiburg, Miscible droplets in a porous medium and the effects of Korteweg stresses, Phys. Fluids **13**, 2447 (2001).

[15] C.-Y. Chen and E. Meiburg, Miscible displacements in capillary tubes: Influence of Korteweg stresses and divergence effects, Phys. Fluids **14**, 2052 (2002).

[16] S. Swernath, B. Malengier, and S. Pushpavanam, Effect of Korteweg stress on viscous fingering of solute plugs in a porous medium, Chem. Eng. Sci. **65**, 2284 (2010).

[17] D. Truzzolillo, S. Mora, C. Dupas, and L. Cipelletti, Off-Equilibrium Surface Tension in Colloidal Suspensions, Phys. Rev. Lett. **112**, 128303 (2013).

[18] W. Henry, Experiments on the quantity of gases absorbed by water, at different temperatures, and under different pressures, Phil. Trans. R. Soc. Lond. A **93**, 29 (1803).

[19] F. M. Orr, *Theory of Gas Injection Processes* (Tie-Line Publications, Copenhagen, Denmark, 2007).

[20] S. Li, J. S. Lowengrub, J. Fontana, and P. Palffy-Muhoray, Control of Viscous Fingering Patterns in a Radial Hele-Shaw Cell, Phys. Rev. Lett. **102**, 174501 (2009).

[21] C.-Y. Chen, C. W. Huang, L. C. Wang, and J. A. Miranda, Controlling radial fingering patterns in miscible confined flows, Phys. Rev. E **82**, 056308 (2010).

[22] T. T. Al-Housseiny, P. A. Tsai, and H. A. Stone, Control of interfacial instabilities using flow geometry, Nat. Phys. **8**, 747 (2012).

[23] D. Pihler-Puzović, P. Illien, M. Heil, and A. Juel, Suppression of Complex Finger-Like Patterns at the Interface Between Air and a Viscous Fluid by Elastic Membranes, Phys. Rev. Lett. **108**, 074502 (2012).

[24] Y. Nagatsu, Y. Ishii, Y. Tada, and A. De Wit, Hydrodynamic Fingering Instability Induced by a Precipitation Reaction, Phys. Rev. Lett. **113**, 024502 (2014).

[25] T. J. Ober, D. Foresti, and J. A. Lewis, Active mixing of complex fluids at the microscale, Proc. Natl. Acad. Sci. USA **112**, 12293 (2015).

[26] C. P. Brangwynne, P. Tompa, and R. V. Pappu, Polymer physics of intracellular phase transitions, Nat. Phys. **11**, 899 (2015).

[27] M. J. Martinez and M. A. Hesse, Two-phase convective CO_2 dissolution in saline aquifers, Water Resour. Res. **52**, 585 (2016).

[28] R. Suzuki, Y. Nagatsu, M. Mishra, and T. Ban, Experimental study on viscous fingering with partial miscible fluids, 69th Annual Meeting of the APS Division of Fluid Dynamics, 2016.

[29] C.-Y. Chen and P.-Y. Yan, A diffuse interface approach to injection-driven flow of different miscibility in heterogeneous porous media, Phys. Fluids **27**, 083101 (2015).

[30] J. W. Cahn and J. E. Hilliard, Free energy of a nonuniform system, I: Interfacial free energy, J. Chem. Phys. **28**, 258 (1958).

[31] G. Tryggvason and H. Aref, Numerical experiments on Hele-Shaw flow with a sharp interface, J. Fluid Mech. **136**, 1 (1983).

[32] E. Meiburg and G. M. Homsy, Nonlinear unstable viscous fingers in Hele-Shaw flows, II: Numerical simulation, Phys. Fluids **31**, 429 (1988).

[33] A. Lindner, D. Bonn, E. Poiré Corvera, M. Ben Amar, and J. Meunier, Viscous fingering in non-Newtonian fluids, J. Fluid Mech. **469**, 237 (2002).

[34] S. Nguyen, R. Folch, V. K. Verma, H. Henry, and M. Plapp, Phase-field simulations of viscous fingering in shear-thinning fluids, Phys. Fluids **22**, 103102 (2010).

[35] L. Cueto-Felgueroso and R. Juanes, Macroscopic Phase-Field Model of Partial Wetting: Bubbles in a Capillary Tube, Phys. Rev. Lett. **108**, 144502 (2012).

[36] L. Cueto-Felgueroso and R. Juanes, A phase-field model of two-phase Hele-Shaw flow, J. Fluid Mech. **758**, 522 (2014).

[37] P. Petitjeans and T. Maxworthy, Miscible displacements in capillary tubes, part 1: Experiments, J. Fluid Mech. **326**, 37 (1996).

[38] C. Y. Chen and E. Meiburg, Miscible displacements in capillary tubes, part 2: Numerical simulations, J. Fluid Mech. **326**, 57 (1996).

[39] Z. Yang and Y. C. Yortsos, Asymptotic solutions of miscible displacements in geometries of large aspect ratio, Phys. Fluids **9**, 286 (1997).

[40] A. Aubertin, G. Gauthier, J. Martin, D. Salin, and L. Talon, Miscible viscous fingering in microgravity, Phys. Fluids **21**, 054107 (2009).

[41] R. M. Oliveira and E. Meiburg, Miscible displacements in Hele-Shaw cells: Three-dimensional Navier-Stokes simulations, J. Fluid Mech. **687**, 431 (2011).

[42] R. M. Oliveira and E. Meiburg, Saffman-Taylor Instability and the Inner Splitting Mechanism, Phys. Rev. Lett. **118**, 124502 (2017).

[43] P. Aussillous and D. Quéré, Quick deposition of a fluid on the wall of a tube, Phys. Fluids **12**, 2367 (2000).

[44] B. Levaché and D. Bartolo, Revisiting the Saffman-Taylor Experiment: Imbibition Patterns and Liquid-Entrainment Transitions, Phys. Rev. Lett. **113**, 044501 (2014).

[45] B. Zhao, C. W. MacMinn, and R. Juanes, Wettability control on multiphase flow in patterned microfluidics, Proc. Natl. Acad. Sci. USA **113**, 10251 (2016).

[46] D. M. Anderson, G. B. McFadden, and A. A. Wheeler, Diffuse-interface methods in fluid mechanics, Annu. Rev. Fluid Mech. **30**, 139 (1998).

[47] R. Folch, J. Casademunt, A. Hernández-Machado, and L. Ramirez-Piscina, Phase-field models for Hele-Shaw flows with arbitrary viscosity contrast, I: Theoretical approach, Phys. Rev. E **60**, 1724 (1999).

[48] R. Folch, J. Casademunt, A. Hernández-Machado, and L. Ramirez-Piscina, Phase-field models for Hele-Shaw flows with arbitrary viscosity contrast, II: Numerical study, Phys. Rev. E **60**, 1734 (1999).

[49] A. Hernández-Machado, A. M. Lacasta, E. Mayoral, and E. Corvera-Poiré, Phase-field model of Hele-Shaw flows in the high-viscosity contrast regime, Phys. Rev. E **68**, 046310 (2003).

[50] H.-G Lee, J. S. Lowengrub, and J. Goodman, Modeling pinchoff and reconnection in a Hele-Shaw cell, I: The models and their calibration, Phys. Fluids **14**, 492 (2002).

[51] H.-G Lee, J. S. Lowengrub, and J. Goodman, Modeling pinchoff and reconnection in a Hele-Shaw cell, II: Analysis and simulation in the nonlinear regime, Phys. Fluids **14**, 514 (2002).

[52] Y. Sun and C. Beckermann, A two-phase diffuse-interface model for Hele-Shaw flows with large property contrasts, Phys. D (Amsterdam, Neth.) **237**, 3089 (2008).

[53] L. Cueto-Felgueroso and R. Juanes, Nonlocal Interface Dynamics and Pattern Formation in Gravity-Driven Unsaturated Flow through Porous Media, Phys. Rev. Lett. **101**, 244504 (2008).

[54] X. Fu, L. Cueto-Felgueroso, and R. Juanes, Thermodynamic coarsening arrested by viscous fingering in partial-miscible binary mixtures, Phys. Rev. E **94**, 033111 (2016).

[55] R. Ruiz and D. R. Nelson, Turbulence in binary fluid mixtures, Phys. Rev. A **23**, 3224 (1981).

[56] A. J. Wagner and J. M. Yeomans, Breakdown of Scale-Invariance in the Coarsening of Phase-Separating Binary Fluids, Phys. Rev. Lett. **80**, 1429 (1998).

[57] Z. Shou and A. Chakrabarti, Ordering of viscous liquid mixtures under a steady shear flow, Phys. Rev. E **61**, R2200(R) (2000).

[58] L. Berthier, J.-L. Barrat, and J. Kurchan, Phase Separation in a Chaotic Flow, Phys. Rev. Lett. **86**, 2014 (2001).

[59] S. Berti, G. Boffetta, M. Cencini, and A. Vulpiani, Turbulence and Coarsening in Active and Passive Binary Mixtures, Phys. Rev. Lett. **95**, 224501 (2005).

[60] P. Perlekar, R. Benzi, H. J. H. Clercx, D. R. Nelson, and F. Toschi, Spinodal Decomposition in Homogeneous and Isotropic Turbulence, Phys. Rev. Lett. **112**, 014502 (2014).

[61] W. J. Boettinger, J. A. Warren, C. Beckermann, and A. Karma, Phase-field simulation of solidification, Annu. Rev. Mater. Res. **32**, 163 (2002).

[62] P. C. Hohenberg and B. I. Halperin, Theory of dynamic critical phenomena, Rev. Mod. Phys. **49**, 435 (1977).

[63] S. M. Allen and J. W. Cahn, A microscopic theory for antiphase boundary motion and its application to antiphase domain coarsening, Acta Metall. **27**, 1085 (1979).

[64] A. A. Wheeler, W. J. Boettinger, and G. B. McFadden, Phase-field model of solute trapping during solidification, Phys. Rev. E **47**, 1893 (1993).

[65] G. M. Wilson, Vapor-Liquid Equilibrium. XI. A new expression for the excess free energy of mixing, J. Am. Chem. Soc. **86**, 127 (1964).

[66] A. J. Bray, Theory of phase ordering kinetics, Adv. Phys. **43**, 357 (1994).

[67] T. P. Witelski, The structure of internal layers for unstable nonlinear diffusion equations, Stud. Appl. Math. **97**, 277 (1996).

[68] P. A. Witherspoon and D. N. Saraf, Diffusion of methane, ethane, propane, and n-butane, J. Phys. Chem. **69**, 3752 (1965).

[69] A. L. Bertozzi, N. Ju, and H.-W. Lu, A biharmonic-modified forward time stepping method for fourth order nonlinear diffusion equations, J. Discrete Continuous Dyn. Syst. **29**, 1367 (2011).

[70] T. Maxworthy, Bubble formation, motion, and interaction in a Hele-Shaw cell, J. Fluid Mech. **173**, 95 (1986).

[71] J. V. Maher, Development of Viscous Fingering Patterns, Phys. Rev. Lett. **54**, 1498 (1985).

[72] C. W. Park and G. M. Homsy, The instability of long fingers in Hele-Shaw flows, Phys. Fluids **28**, 1583 (1985).

[73] A. Arnéodo, Y. Couder, G. Grasseau, V. Hakim, and M. Rabaud, Uncovering the Analytical Saffman-Taylor Finger in Unstable Viscous Fingering and Diffusion-Limited Aggregation, Phys. Rev. Lett. **63**, 984 (1989).

[74] G. Daccord and R. Lenormand, Fractal patterns from chemical dissolution, Nature (London) **325**, 41 (1987).

[75] A. De Wit, Fingering of Chemical Fronts in Porous Media, Phys. Rev. Lett. **87**, 054502 (2001).

[76] P. Szymczak and A. J. C. Ladd, The initial stages of cave formation: Beyond the one-dimensional paradigm, Earth Planet. Sci. Lett. **301**, 424 (2011).

[77] F. Haudin, J. H. E. Cartwright, F. Brau, and A. De Wit, Spiral precipitation patterns in confined chemical gardens, Proc. Natl. Acad. Sci. USA **111**, 17363 (2014).

[78] E. O. Dias, E. Alvarez-Lacalle, M. S. Carvalho, and J. A. Miranda, Minimization of Viscous Fluid Fingering: A Variational Scheme for Optimal Flow Rates, Phys. Rev. Lett. **109**, 144502 (2012).

[79] H. Zhao, J. Casademunt, C. Yeung, and J. V. Maher, Perturbing Hele-Shaw flow with a small gap gradient, Phys. Rev. A **45**, 2455 (1992).